Available online at www.sciencedirect.com
SCIENCE DIRECT®
International Journal of Heat and Mass Transfer 48 (2005) 341–359
International Journal of HEAT and MASS TRANSFER
www.elsevier.com/locate/ijhmt

Experimental and large eddy simulation results for the purging of salt water from a cavity by an overflow of fresh water

M.P. Kirkpatrick *, S.W. Armfield

School of Aerospace, Mechanical and Mechatronic Engineering, The University of Sydney, Sydney, NSW 2006, Australia

Received 17 July 2003; received in revised form 20 July 2004

Abstract

This paper presents the results of an experimental and numerical investigation of a flow in which salt water is purged from a square cavity by an overflow of fresh water. Two numerical simulations are presented, one two-dimensional simulation and one three-dimensional large eddy simulation. The results are used to describe the important transport mechanisms that occur during the purging process. In particular, we propose a mechanism for the formation of the streamers observed in the experiment. We also discuss the performance of the numerical models for flows of this type.

Keywords: Purging; Stratified flow; Large eddy simulation; Density interface, Turbulent entrainment

1. Introduction

Turbulent mixing and transport in stratified media are fundamental mechanisms in many environmental and industrial flows, occurring in lakes, estuaries, the oceans, the atmosphere, heat exchangers, and many other settings. The study of the fluid mechanics associated with such flows is an active focus of the international research community and consequently the literature is vast. A few notable examples are the recent work of Smyth and Moum [1,2] who used DNS to analyse turbulence resulting from a Kelvin–Helmholtz instability, and Fernando and Hunt [3] and McGrath et al. [4] who combined theoretical and experimental analysis to investigate waves, turbulence and mixing at density interfaces. The reader is referred to review papers of Gregg [5], Fernando [6], Caldwell and Moum [7] and Riley and Lelong [8] for a more complete discussion of advances made in this area.

An example of density-stabilised flow that has important environmental significance is the purging of salt water from a cavity by an overflow of fresh water. Saline pools, formed by ground water intrusion through the river bed during periods of low flow, occur in many of the world's rivers and can lead to major environmental problems. In Australia, for instance, Anderson and Morrison [9] carried out a number of studies identifying the adverse effects of high salinities. They observed that density-stratified saline pools are formed during periods of low flow. The pools consist of an upper layer of fresh water and a lower layer of salt water, typically contained in a scour hole in the river. Water quality in these saline pools is often very poor with low levels of dissolved oxygen, and salinities exceeding 20,000 EC units (13,680 ppm).

* Corresponding author. Present address: School of Engineering, University of Tasmania, Private Bag 65, Hobart 7001, Australia. Tel.: +61 3 6226 7639; fax: +61 3 6226 7247.
E-mail address: michael.kirkpatrick@utas.edu.au (M.P. Kirkpatrick).

0017-9310/$ - see front matter © 2004 Elsevier Ltd. All rights reserved.
doi:10.1016/j.ijheatmasstransfer.2004.08.016

Nomenclature

c	mixture fraction
C	Dynamic Smagorinsky model coefficient
C_s	Classical Smagorinsky model coefficient
CFL	Courant–Friedrich–Lévy number
Fr	densimetric Froude number
g	acceleration due to gravity
H	minimum interface height
H^*	mean interface height
H_{cav}	cavity height
H_{chan}	channel height
K_{EF}	coefficient in purging parameterisation
L	interface length
P	pressure
Pr	Prandtl number
Q	amount of solute remaining in cavity
Ra	Rayleigh number
Re	Reynolds number
S_{ij}	strain rate tensor
t	time
U	free stream velocity
u_i	Cartesian components of velocity vector
x_i	Cartesian components of position vector

Greek symbols

α	ratio of test filter to grid filter
γ	subgrid scale scalar flux
δ_τ	length scale for non-dimensional wall units
δ_{ij}	Kronecker delta
$\overline{\Delta}$	grid filter width
κ	kinematic diffusivity of salt
ν	kinematic viscosity
ϱ	density
ϱ_f	initial density of fresh water
ϱ_s	initial density of salt water
$\Delta\varrho$	density differential ($=(\varrho - \varrho_f)/\varrho_f$)
σ	concentration of salt
τ_{ij}	subgrid scale stress tensor
τ_w	wall shear stress

Superscripts

$\overline{\ }$	grid filter
$\widehat{\ }$	test filter
$+$	non-dimensional wall units

Subscripts

0	initial conditions
sgs	subgrid scale

When the pools are subjected to a sufficiently large fresh overflow, as a result of heavy rainfall or the release of water from upstream storage, the overflow purges the pool of salt water. The factor controlling the speed of this purging process is the rate at which the denser salt water is transported against a downward buoyancy force into the fresh water above. In order to maintain the integrity of the river systems it is necessary to understand the flow dynamics of the water within the pools during the purging flows [10]. This information will allow the accurate determination of the flow regimes required to purge pools of saline water, which in turn will be of great benefit in implementing effective river management, salt drainage and salt disposal strategies.

Problems resulting from increased salinity levels in river systems are by no means confined to Australian river systems. Irrigation for farming has resulted in a salinity problem in the Colorado River, while on the River Danube, Gill [11] identified flows similar to those considered here associated with mining pits in the river. In Greece [12], Rotterdam [13] and Valdivia in Chile [14], the mixing of tidal salt water intrusions in estuaries is of concern.

In 1993, Armfield and Debler [15] carried out experimental and numerical investigations of purging of salt water from a square cavity. Two-dimensional, direct numerical simulations were performed using a finite volume unsteady Navier–Stokes code with geometry matching that of the laboratory facility. Their results indicate that the purging process can be characterised in terms of the Reynolds number of the overflow and the Rayleigh number based on the initial density variation. In subsequent work [16], the investigation was extended to rectangular and trapezoidal cavities with a range of aspect ratios (length:depth) ranging from 1:1 to 10:1. Reynolds numbers based on the flow depth were in the range 1000–10,000.

The purging process is initiated by an impulsive start, which generates an initial splash followed by a large vortex that traverses the interface between the fresh and salt water. On reaching the downstream side of the cavity, the vortex draws fresh water down into the cavity, destabilising the dense fluid. Large-scale flow features generated by this impulsive start cause rapid purging during the early stages of the process. At later times, however, these features subside and a new transport mechanism becomes important. The fresh water flowing above the

almost-static salt water generates small waves on the interface. Periodically, streamers of dense fluid are ejected from the crests of the waves and are then carried away by the turbulent overflow. This process is unidirectional, that is, it results only in the transport of saline solution up into the fresh overflow and does not transport fresh fluid down into the relatively static saline solution. As a result, the process maintains the sharp interface, which slowly drops as saline fluid is removed from the pool.

Using the assumption that the rate of work done on the interface to remove saline fluid from the basin is balanced by the flux of turbulent kinetic energy into the cavity, Debler and Armfield [16] derived a parameterisation for the purging rate,

$$\frac{(\mathrm{d}Q^*/\mathrm{d}t)}{UFr^2} = \frac{K_{EF}(H_{\mathrm{chan}}/L)}{(1-H^*/H_{\mathrm{cav}})([1+H_{\mathrm{cav}}/H_{\mathrm{chan}}]-H^*/H_{\mathrm{chan}})^2}, \tag{1}$$

where $\mathrm{d}Q^*/\mathrm{d}t$ is the rate of purging per unit interface area, U the free-stream velocity, Fr the densimetric Froude number, H_{chan} the channel height, H_{cav} the cavity height, H^* the mean interface height, L interface length, and K_{EF} a model coefficient. The relation gives excellent prediction of the purging rate for high aspect ratio cavities, indicating that the interfacial waves and streamers constitute the dominant transport mechanism for long cavities. It is also likely to be the dominant mechanism in natural riverine ponds, which are typically of high aspect ratio.

While the 2D direct numerical simulations reported in [15] accurately predicted the initial wave and seiching, they performed very poorly for the remaining part of the process, giving a substantial under-prediction of the purging rate. The streamers ejected by the breaking interfacial waves are of order 1 mm in width, and currently cannot be accurately resolved on any computationally feasible grid. It is therefore necessary to use a turbulence model of some sort to obtain accurate prediction of the turbulent transport. Craft et al. [17] tested a k–ϵ model with a Richardson number correction for a similar flow and found that it provided very poor prediction, almost immediately diffusing the interface and over-predicting the purging rate by more than an order of magnitude.

This paper presents an experiment, a two-dimensional simulation, and a three-dimensional large eddy simulation of purging of salt water from a cavity. The experiment is similar to those of Armfield and Debler. For the present work, however, we have chosen a set of flow parameters that enable us to run the large eddy simulation at high spatial resolution. Simulations are performed with the large eddy simulation code, PUFFIN [18]. The experimental and numerical results are used to describe the important transport mechanisms that occur during the the purging process. In particular, we propose a mechanism for the formation of the streamers observed in the previous work described above. We also discuss the performance of the numerical models for flows of this type.

2. Experimental method

The aims of the experiment are to measure the rate at which saline solution in a square cavity is purged by a turbulent overflow of fresh water, and to visualise the flow field during the process. The non-dimensional parameters used to define the flow are the Reynolds number and Rayleigh number, defined here as

$$Re = \frac{UH_{\mathrm{chan}}}{\nu}; \quad Ra = \frac{gH_{\mathrm{chan}}^3 \Delta\varrho_0}{\nu\kappa}. \tag{2}$$

Another useful parameter is the Froude number,

$$Fr = \left(\frac{Re^2 Pr}{RaH_{\mathrm{cav}}/H_{\mathrm{chan}}}\right)^{1/2}. \tag{3}$$

Here U is the velocity at the free surface of the channel, H_{chan} the height of the water in the channel, H_{cav} the height of the cavity, and g the acceleration due to gravity. The density differential between the fresh and salt water is $\Delta\varrho_0 = (\varrho_{\mathrm{s}} - \varrho_{\mathrm{f}})/\varrho_{\mathrm{f}}$, where ϱ_{f} and ϱ_{s} are the initial densities of the fresh and salt water, respectively. The kinematic viscosity of water is ν and the kinematic diffusion coefficient for salt is $\kappa = \nu/Pr$, where Pr is the Prandtl number, taken as 750. The values of the non-dimensional parameters chosen for the experiment are $Re \approx 7500$, $Ra = 6.5 \times 10^9$, $Fr = 2.2$. The corresponding dimensional parameters are

$$\begin{aligned} &U = 0.1\ \mathrm{m/s}; \quad \varrho_{\mathrm{f}} = 1000.0\ \mathrm{kg/m^3};\\ &\Delta\varrho = 0.22\%; \quad H_{\mathrm{chan}} = 0.075\ \mathrm{m}; \quad H_{\mathrm{cav}} = 0.1\ \mathrm{m};\\ &\nu = 1.0 \times 10^{-6}\ \mathrm{m^2/s}; \quad \kappa = 1.33 \times 10^{-9}\ \mathrm{m^2/s}. \end{aligned} \tag{4}$$

The experimental apparatus is shown in Fig. 1. The apparatus consists of a flume 54 mm wide and 200 mm high and 2 m long containing a false floor into which is set a square cavity. The side-length of the cavity is 100 mm. An overflow weir is installed at the downstream end of the flume and the upstream end is sealed shut to form a rectangular basin. The top of the overflow weir is 65 mm above the false floor. With a free-surface velocity of 0.1 m/s, the height of the water level above the top of the weir is approximately 10 mm giving a total height of 75 mm in the channel.

Fresh water for the experiment is supplied at the upstream end of the flume. A plastic gauze placed in the channel acts as a flow straightener to damp large-scale disturbances. The concentration of salt in the saline solution is measured using a conductivity meter and is checked by measuring the specific gravity of the solution

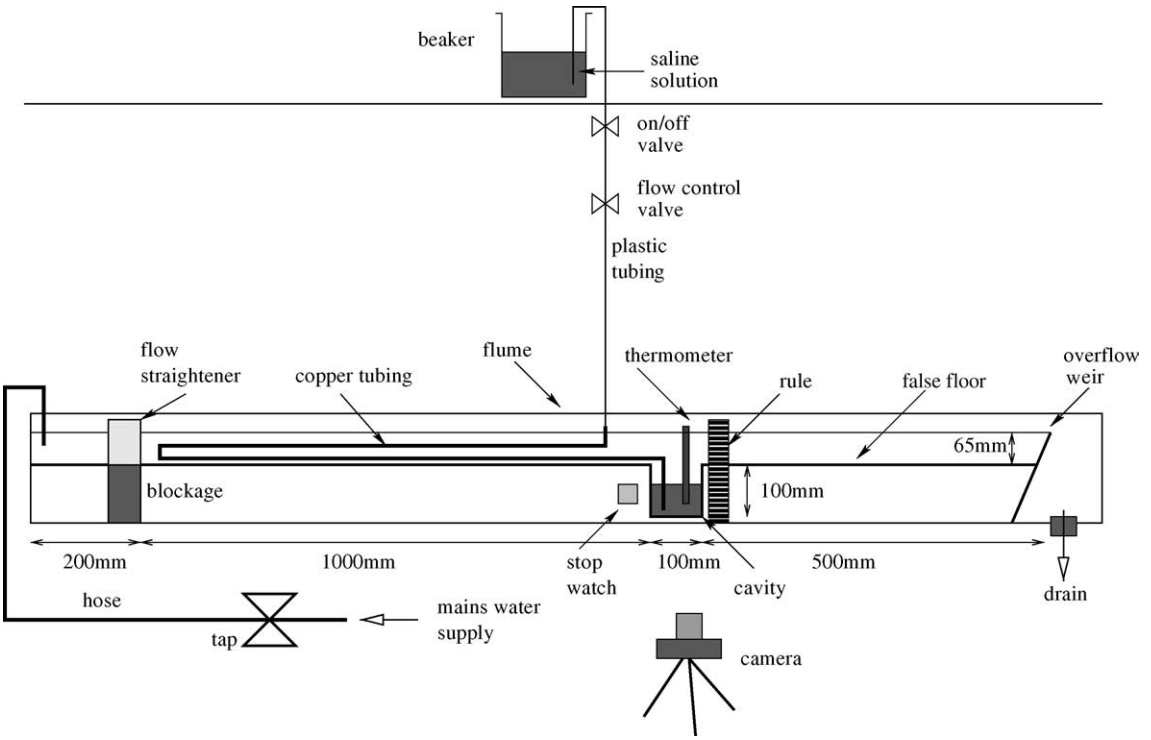

Fig. 1. Schematic showing rig used for the purging cavity experiment.

using a hydrometer. Blue dye is added to the solution to enable visualisation of the salt concentration field during the experiment. The dye was shown to have no significant effect on the density of the water. At a temperature of $T = 20\,^{\circ}\mathrm{C}$, a temperature difference of $\Delta T = 1\,\mathrm{K}$ corresponds to a density difference $\Delta\varrho \approx 0.018\%$, which is approximately 10% of the density difference due to the solute. This is taken as the maximum allowable temperature variation during the experiment.

Before each experiment, the flume is flushed with fresh water at 20 °C for around 15 min to bring the temperature of the perspex walls to the same temperature. With the flume initially filled with fresh water, the saline solution is then introduced slowly into the cavity. The solution is conveyed through a copper tube that runs twice along the flume before entering the cavity. This ensures that the saline solution is brought to the same temperature as the fresh water in the flume. Filling the cavity takes around 20 min to complete. During this time the temperature of the water in the cavity is monitored to make sure it does not exceed the prescribed error limits. Once the cavity is filled with saline solution, the tube is removed and the thermometer is moved to a position downstream of the cavity.

At the start of the experimental run, a valve on the freshwater supply is turned rapidly to a pre-calibrated position. The parameters recorded during the run are the height, temperature and the velocity of the water in the channel. The velocity is measured by recording the time taken for a drop of dye to travel 1 m along the channel at half the channel height. The free-surface velocity is then found by assuming a 1/7th power law velocity profile. Here, measurements were repeated three times and were found to vary by less than 5%. The range of parameters recorded during the experimental runs are summarised in Table 1.

Table 1
The range of parameters recorded during the cavity flow experiment

Parameter	Description	Mean	Range
U	Free surface velocity (m/s)	0.105	0.099–0.110
$\Delta\varrho_0$	Density difference (%)	0.22	0.216–0.223
ΔT	Temperature difference (K)	0.5	0.0–1.0
H_{chan}	Surface height (mm)	75	74–76

3. Numerical simulations

3.1. Governing equations

The governing equations are the spatially filtered equations for conservation of momentum, mass, solute

concentration and an equation of state. The filtered equations for conservation of mass and momentum for an incompressible liquid with small variations in density are written in Cartesian tensor form as

$$\frac{\partial \overline{u}_j}{\partial x_j} = 0, \tag{5}$$

$$\frac{\partial \overline{u}_i}{\partial t} + \frac{\partial (\overline{u}_i \overline{u}_j)}{\partial x_j} = -\frac{1}{\varrho_f}\frac{\partial \overline{P}}{\partial x_i} + \frac{\partial}{\partial x_j}\left(2\nu \overline{S}_{ij}\right) + \Delta\varrho g_i - \frac{\partial \tau_{ij}}{\partial x_j}. \tag{6}$$

Here the overbar ($\overline{\ }$) is the spatial filtering operator, u_i are the Cartesian components of the velocity vector $\boldsymbol{u}$, x_i are the Cartesian components of the position vector $\boldsymbol{x}$, P is the pressure, ν the kinematic molecular viscosity, g_i the acceleration due to gravity and $\overline{S}_{ij}$ the large-scale strain rate tensor,

$$\overline{S}_{ij} = \frac{1}{2}\left(\frac{\partial \overline{u}_i}{\partial x_j} + \frac{\partial \overline{u}_j}{\partial x_i}\right). \tag{7}$$

The last term in Eq. (6) is the subgrid scale or SGS stress tensor,

$$\tau_{ij} = \overline{u_i u_j} - \overline{u}_i \overline{u}_j. \tag{8}$$

The Smagorinsky model [19] is used to parameterise the subgrid scale stress tensor,

$$\tau_{ij} - \frac{1}{3}\delta_{ij}\tau_{kk} = -2\nu_{\mathrm{sgs}}\overline{S}_{ij}. \tag{9}$$

Here the eddy viscosity ν_{sgs} is a function of the filter size and the strain rate,

$$\nu_{\mathrm{sgs}} = C\overline{\Delta}^2|\overline{S}|, \tag{10}$$

where $|\overline{S}| = \sqrt{2\overline{S}_{ij}\overline{S}_{ij}}$ and C is the dimensionless model coefficient. The dynamic procedure of Germano et al. [20] is used to calculate the model coefficient and length scale. The procedure involves the application of a test filter ($\widehat{\ }$) to the velocity field to obtain information about the smallest resolved scales. Comparison of the grid and test filtered fields gives an expression for the required parameters,

$$C\overline{\Delta}^2 = -\frac{\mathscr{L}_{ij}M_{ij}}{2M_{ij}M_{ij}}, \tag{11}$$

where

$$\mathscr{L}_{ij} = \widehat{\overline{u}_i\overline{u}_j} - \widehat{\overline{u}}_i\widehat{\overline{u}}_j \tag{12}$$

and

$$M_{ij} = \alpha^2|\widehat{\overline{S}}|\widehat{\overline{S}}_{ij} - \widehat{|\overline{S}|\overline{S}_{ij}}, \quad \alpha = \widehat{\overline{\Delta}}/\overline{\Delta}. \tag{13}$$

Substituting these relations into Eq. (6) gives

$$\frac{\partial \overline{u}_i}{\partial t} + \frac{\partial (\overline{u}_i \overline{u}_j)}{\partial x_j} = -\frac{1}{\varrho_f}\frac{\partial \overline{P}}{\partial x_i} + \frac{\partial}{\partial x_j}\left(2\left(\nu + \nu_{\mathrm{sgs}}\right)\overline{S}_{ij}\right) + \Delta\varrho g_i. \tag{14}$$

The solute concentration σ in the mixture is normalised by the initial concentration of unmixed saline solution in the cavity σ_0 to give the mixture fraction

$$c = \frac{\sigma}{\sigma_0}. \tag{15}$$

The transport of solute concentration is then governed by the equation

$$\frac{\partial \overline{c}}{\partial t} + \frac{\partial (\overline{u}_j \overline{c})}{\partial x_j} = \frac{\partial}{\partial x_j}\left[\frac{\nu}{Pr}\frac{\partial \overline{c}}{\partial x_j}\right] - \frac{\partial \gamma}{\partial x_j}. \tag{16}$$

Here the diffusion coefficient κ has been written in terms of the dynamic viscosity ν and a Prandtl number Pr which for salt water is taken as 750.

The SGS scalar flux

$$\gamma = \overline{u_j c} - \overline{u}_j \overline{c} \tag{17}$$

is approximated using the eddy viscosity calculated for the velocities and a subgrid scale turbulent Prandtl number,

$$\gamma \approx -\frac{\nu_{\mathrm{sgs}}}{Pr_{\mathrm{sgs}}}\frac{\partial \overline{c}}{\partial x_j}, \tag{18}$$

where $Pr_{\mathrm{sgs}} = 1.0$. Substituting into Eq. (16), the filtered equation for the mixture fraction becomes

$$\frac{\partial \overline{c}}{\partial t} + \frac{\partial (\overline{u}_j \overline{c})}{\partial x_j} = \frac{\partial}{\partial x_j}\left[\left(\frac{\nu}{Pr} + \frac{\nu_{\mathrm{sgs}}}{Pr_{\mathrm{sgs}}}\right)\frac{\partial \overline{c}}{\partial x_j}\right]. \tag{19}$$

The density differential of the mixture is calculated from the mixture fraction using an equation of state,

$$\Delta\varrho = \overline{c}\Delta\varrho_0. \tag{20}$$

3.2. Numerical solution of equations

The equations are discretised in space using a finite volume formulation on a non-uniform, staggered, Cartesian grid. The computational domain, coordinate directions and grid are shown in Fig. 2. The upstream boundary condition is an inflow boundary with a steady 1/7th power-law velocity profile and zero salt concentration. The use of a steady inflow condition is justified here as Armfield and Debler (personal communication) found experimentally that the rate of purging is insensitive to the turbulence intensity in the channel. The downstream boundary uses a zero-normal-gradient outflow boundary condition for velocity and salt concentration. In the 3D simulation, the spanwise boundaries are periodic for all variables.

The spanwise dimension of the domain (30 mm) was chosen to correspond to the wavelength of the largest flow structures estimated from experimental observations. This dimension corresponds to $x^+ \approx 100$ where $x^+ = x/\delta_\tau$ and δ_τ is estimated from the mean shear stress of $\tau_w \approx 1.0 \times 10^{-2}\,\mathrm{N/m^2}$ measured in the numerical simulations on the section of the downstream wall above

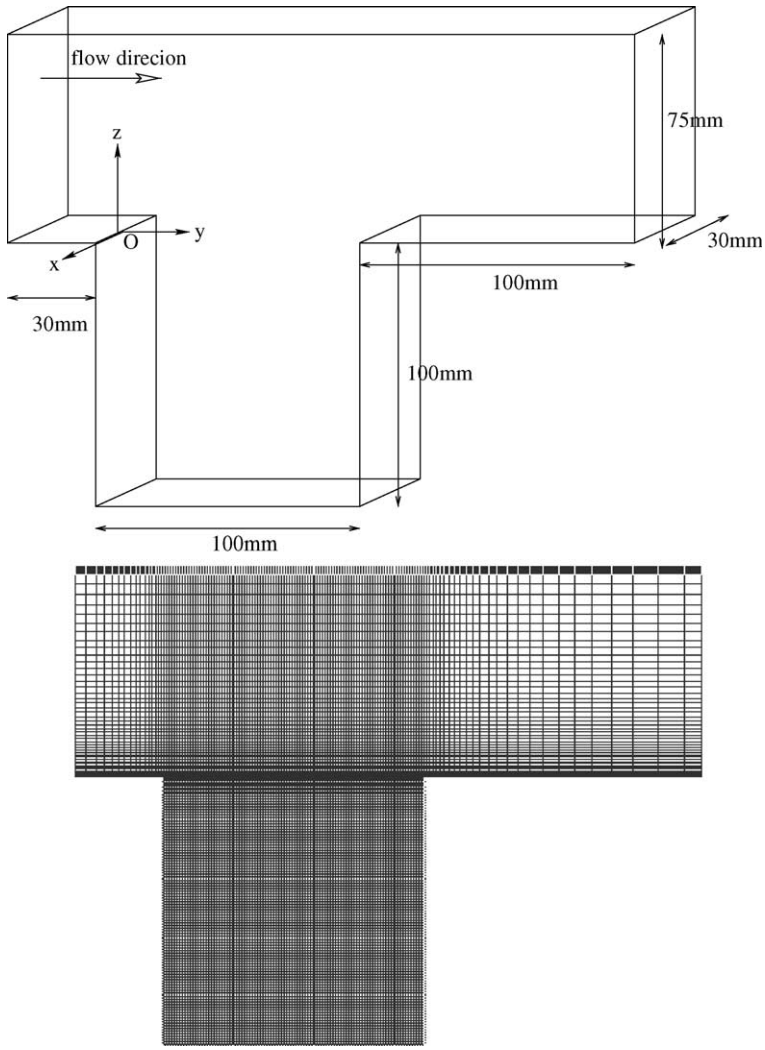

Fig. 2. Computational domain and grid for purging cavity.

the interface at $t = 100$ s. This time corresponds approximately to the midpoint in the purging process. Streamwise vortices generated near the wall in a turbulent boundary layer have a spanwise spacing of $x^+ \approx 100$ [21,22], so this domain width is the minimum that will permit the formation of similar vortical structures in the boundary layer along the downstream cavity wall. The solid boundaries use a power-law wall function [23], while the free-surface of the channel is an impermeable, free-slip boundary.

The 3D grid has $15 \times 140 \times 147$ cells in the x, y and z directions respectively with $15 \times 100 \times 120$ cells concentrated within the cavity. Cells within the cavity are of uniform size in the x and y directions with $\Delta x = 2$ mm and $\Delta y = 1$ mm. In the z direction, the cell width is generally $\Delta z = 1$ mm except in the upper part of the cavity where the grid is compressed to give $\Delta z = 0.5$ mm at the top of the cavity. Outside the cavity the grid is expanded in the y and z directions to reduce computation time. The 2D simulation is performed on the same grid with a single cell in the x direction.

The spatial discretisation uses second-order central differences for all terms in the momentum equations and pressure correction equation. Second-order central differences are also used for the diffusion terms in the mixture fraction equation while SHARP [24] is used for the advection terms to prevent numerical oscillations. A detailed discussion of the spatial discretisation scheme is given in [25,18].

In the 3D simulation, the model coefficient field calculated by the standard dynamic procedure varies markedly in time and space. Two techniques are used to reduce these oscillations. The first is the technique recommended by Germano et al. [20] of averaging the con-

tracted tensors in Eq. (11) in homogeneous directions. In this flow, there is only one homogeneous direction, namely the x direction. Breuer [26] found averaging in one direction for vortex-shedding flow past a circular cylinder to be insufficient and used additional time-averaging to help stabilise the model coefficient. In the present work, extra stability is achieved by filtering the velocity field explicitly to remove the high wavenumbers before calculating the coefficient. The filter used for this operation is the same 3D box filter used for the test filtering procedure.

The flow parameters used for the numerical simulations are those listed in Eq. (4). The equations are advanced in time using a fractional step method. First, the mixture fraction equation is integrated in time using a Crank-Nicolson scheme and the solution used to calculate the density field at the end of the time step. Next, the momentum equations are integrated using a third-order hybrid Adams-Bashforth/Adams-Moulton scheme to give an approximate solution for the velocity field. Finally, mass conservation is enforced through a pressure correction step in which the approximate velocity field is projected onto a subspace of divergence free velocity fields. The pressure-correction method of Van Kan [27] and Bell et al. [28] was found to be the fastest of the methods tested by Armfield and Street [29] and is the method used here. Gresho [30] has shown analytically that this method is second-order accurate in time. Verification of the second-order time accuracy of the PUFFIN code, and a more detailed discussion of time-stepping schemes and the fractional step method used here can be found in [31,18]. The time step is varied to keep the maximum CFL number in the range $0.35 < CFL = \Delta t u_i/\Delta x_i < 0.45$, where the dimension Δx_i is the cell width in the direction of the velocity component u_i.

The 2D simulation takes approximately 40 h to complete on a Compaq DS-10. The 3D simulation, which integrates over the time $t = 100 - 200$ s, takes approximately 2 weeks to run on a Compaq DS-10 and uses approximately 250 MB of RAM. Calculations are performed in double-precision. Typical conservation errors per time step for the 3D run calculated as the L_2 norm are: momentum $\sim 5.0 \times 10^{-5}$, mass $\sim 1.0 \times 10^{-9}$, mixture fraction $\sim 5.0 \times 10^{-5}$.

4. Experimental and 2D simulation results

This section presents the results obtained from the experiment and simulations. The experimental results and 2D simulation are first compared for the whole purging process. Results of the 2D and 3D simulations are then compared for the last stage of the process, in which three-dimensional effects are believed to play a dominant role.

4.1. Comparison of purging rate

Fig. 3 shows plots of the minimum interface height H against time as measured in the experiment and the 2D simulation. This parameter was chosen because it is easy to measure accurately from the photographs taken during the experiment. The numerical result is calculated by finding the minimum height at which the mixture fraction is less than 50%. Other parameters, such as the amount of solute in the cavity at a given time, are more difficult to measure from the experimental results as there is a large region on the upstream side of the cavity in which there is a mixture of salt and fresh water. Numerical results for the amount of solute Q remaining in the cavity, and a curve calculated using the theoretical correlation of Debler and Armfield (see Eq. (1)) are also shown in the figure.

Overall, the variation in the experimental results is small, with the measured interface height lying within a range of 5–7 mm at most times. The exception to this is during the period $t = 15 - 45$ s, which shows a range of approximately 15 mm. During this period the results appear to be particularly sensitive to the initial conditions.

The numerical result for interface height is generally in fair agreement with the experimental results, with very good agreement seen during the period $t = 40 - 100$ s. A significant difference is seen in the results at $t = 6$ s. At this time, the interface in the simulation, reaches a minimum of 43 mm and then begins to rise again. The interface in the experiment, on the other hand, continues to drop, reaching a minimum of 31 ± 5 mm at $t = 8 - 10$ s. This offset is gradually reduced so that by $t = 40$ s the two sets of results are again in accord. The experimental data points during this time period are

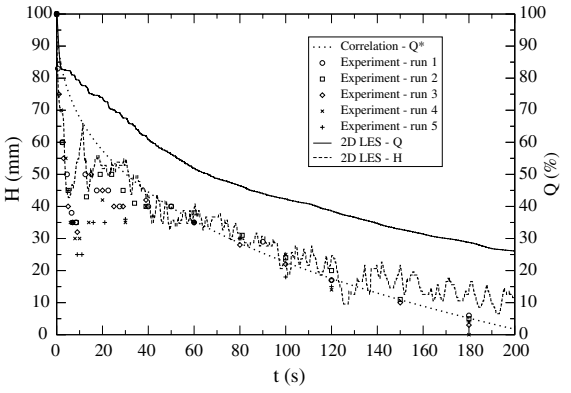

Fig. 3. Comparison of experimental and 2D numerical interface height, H. Also shown are the numerical results for Q—the amount of solute remaining in the cavity, and the theoretical prediction obtained using the correlation of Debler and Armfield [16] with $K_{EF} = 0.024$.

spread over a considerable range, making it difficult to calculate an accurate estimate of the purging rate for this period. During the period $t = 40 - 100$ s the agreement between the two sets of results is remarkable, with the numerical results overlaying the experimental data points. During this period the mean purging rate for both cases is $dH/dt \approx 0.36$ mm/s. After $t = 100$ s the two sets of results begin to diverge again. The mean purging rate measured in the experiment for $t = 100 - 200$ s is $dH/dt \approx 0.23$ mm/s, whereas the simulation predicts $dH/dt \approx 0.16$ mm/s, an underprediction of nearly 30%. The purging rate calculated using dQ/dt correlates well with dH/dt during this stage and gives the same result, that is $dQ/dt = 0.16\% \equiv dH/dt = 0.16$ mm/s. This is a useful result, since it is possible to calculate dQ/dt considerably more accurately than dH/dt.

The theoretical curve for Q is calculated using the correlation of Debler and Armfield discussed in the introduction. Debler and Armfield suggest a value of $K_{EF} = 0.04$ for square cavities. For the present case, a somewhat smaller value of $K_{EF} = 0.024$ was found to give the best fit to the data and the curve shown in the figure uses this value. This difference may be attributed to the different means of determining the interface height. The coefficient value of 0.04 was calibrated based on analysis using the mean interface height rather than the minimum interface height measured in the experiment presented here. With the revised coefficient, the correlation is in very good agreement with the experimental results for $t > 60$ s.

4.2. Flow visualisations

Figs. 4–8 show comparisons of the solute concentration field calculated by the 2D simulation with photographs taken during experiment. The results are compared over the time $t = 0$–200 s. In the following sections the purging process is divided into four stages. For each stage we compare the numerical and experimental results, and use them to identify the mechanisms by which denser fluid is transported across the interface between the salt and fresh water during that stage.

4.2.1. Stage 1: $t = 0$–5 s

Fig. 4 shows the numerical and experimental solute concentration fields during Stage 1. This stage corresponds to the time interval $t = 0$–5 s. The impulsive start-up pushes a large splash of salt water out of the cavity as seen at $t = 0.5$ s. In the simulation, the maximum deflection of the interface from the top of the cavity is 23 mm, which is approximately 15% less than the deflection of 27 mm seen in the experiment. This discrepancy is due to slightly different initial conditions in the two cases. In the experiment the water level starts at the height of the overflow weir, namely 65 mm, and then rises during the first seconds to its equilibrium height of 75 mm. Consequently, the initial flow field in the experiment is amplified by approximately 15%, causing the larger deflection of the interface and a larger ejection of salt water. At the same time as the initial splash, a vortex is formed at the upstream corner of the cavity.

By $t = 2.0$ s the vortex is approximately half way across the cavity. The photograph of the experiment shows turbulent eddies forming as a result of instabilities generated in the shear layer between the vortex and the interface. The eddies are seen lifting the denser salt water into the main vortex. Because the simulation is two-dimensional, it is unable to capture these turbulent motions explicitly and the resolved flow field in the simulation remains laminar. The simulation therefore relies entirely on the turbulence model to parameterise turbulent mixing across the interface. Both the visualisation results and the quantitative comparison of the purging rates discussed in Section 4.1 above, indicate that the turbulence model underpredicts the rate of turbulent mixing during this stage of the process. This is not surprising, since the turbulence model used is generally considered more appropriate for 3D simulations.

At $t = 3.5$ s the vortex reaches the downstream wall and the salt water lifted into the vortex by the turbulent eddies is ejected into the overflow in a second purging event. As expected, this second purging event is underpredicted by the simulation due to its underprediction of turbulent mixing.

The underprediction of both the initial splash and the second purging event result in the divergence of the numerical and experimental purging curves seen at $t = 6$ s in Fig. 3.

4.2.2. Stage 2: $t = 5 - 40$ s

Fig. 5 shows the numerical and experimental solute fields during the first half of Stage 2, corresponding to the time interval $t = 5 - 15$ s. During this time the large vortex draws more fresh water down into the cavity where it interacts with the denser salt water generating Rayleigh-Taylor type instabilities. While some of the vortices generated by these instabilities have a counter-clockwise direction, the vortices shed from the upstream corner of the cavity have a clockwise direction. The interaction of vortices of different directions leads to a highly complex development of the flow field. The end result, however, is that, by $t = 12.3$ s, a counter-clockwise rotating vortex has been forced into the upstream half of the cavity where it begins mixing the fresh and salt water.

Fig. 6 shows the results for the second half of Stage 2, corresponding to the time interval $t = 15$–40 s. At $t = 18$ s, the large clockwise vortex on the right hand side (RHS) of the cavity and the counter-rotating vortex on the left hand side (LHS) of the cavity are seen lifting a large quantity of dense salt water up the centre of the

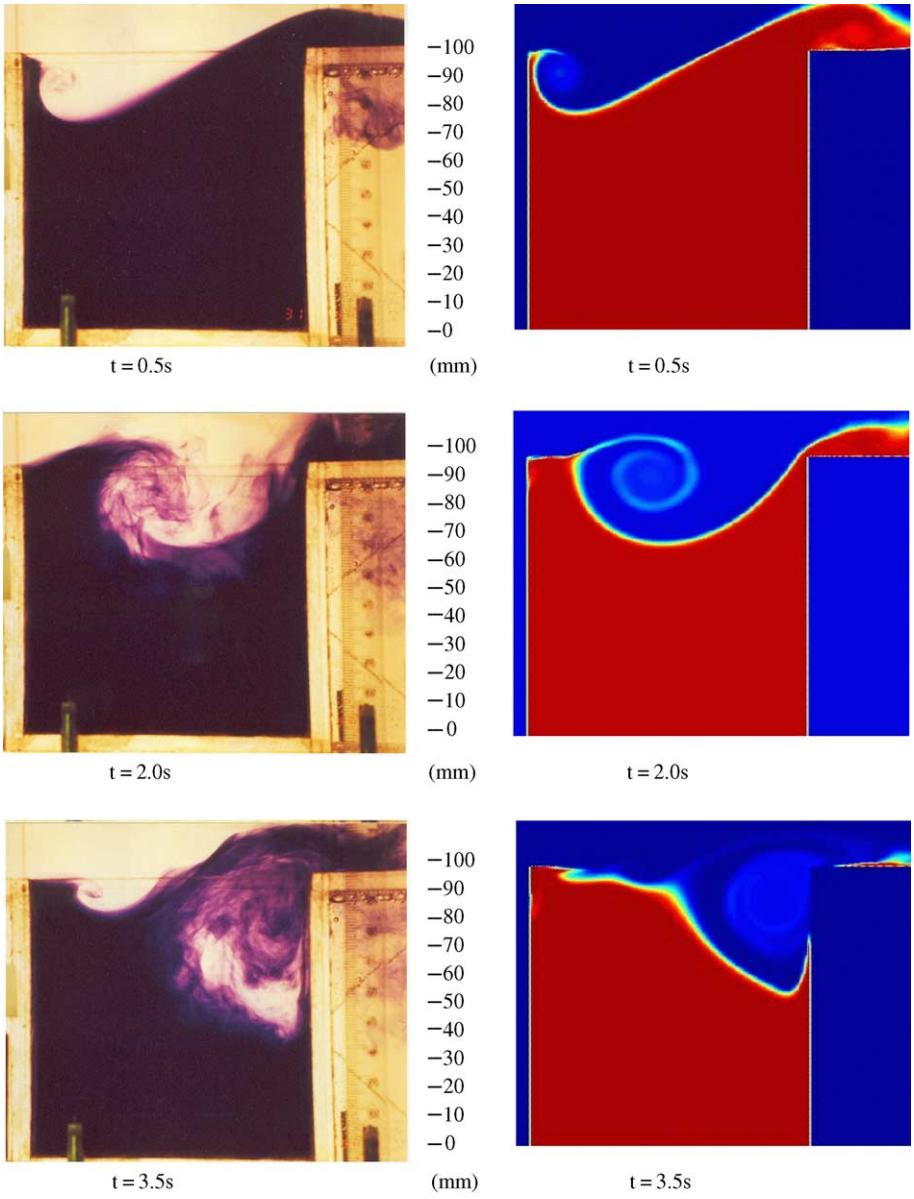

Fig. 4. Stage 1: experimental and 2D numerical solute fields.

cavity to the top, where it is convected away by the overflow. During the remaining part of this stage, these two large vortices gradually grow and become more stable as they remove the denser fluid from below.

A comparison of the numerical and experimental flow fields shows good qualitative agreement during this stage, with similar structures seen in both sets of results. As in the previous stage, the main difference in the results seen is the absence in the numerical results of the small-scale turbulent structures visible in the experimental visualisations.

4.2.3. Stage 3: t = 40–100 s

Fig. 7 shows the numerical and experimental solute fields for Stage 3 corresponding to the time period $t = 40$–100 s. The results show small vortices forming in the shear layer at the top of the cavity. This layer contains both a velocity and a density gradient, and the vortices have the appearance of Kelvin–Helmholtz billows. On reaching the downstream wall, the vortices are deflected downward and impinge on the density interface. In a study of the interaction of vortex rings with a sharp density interface, Linden [32] cites eddy impingement as

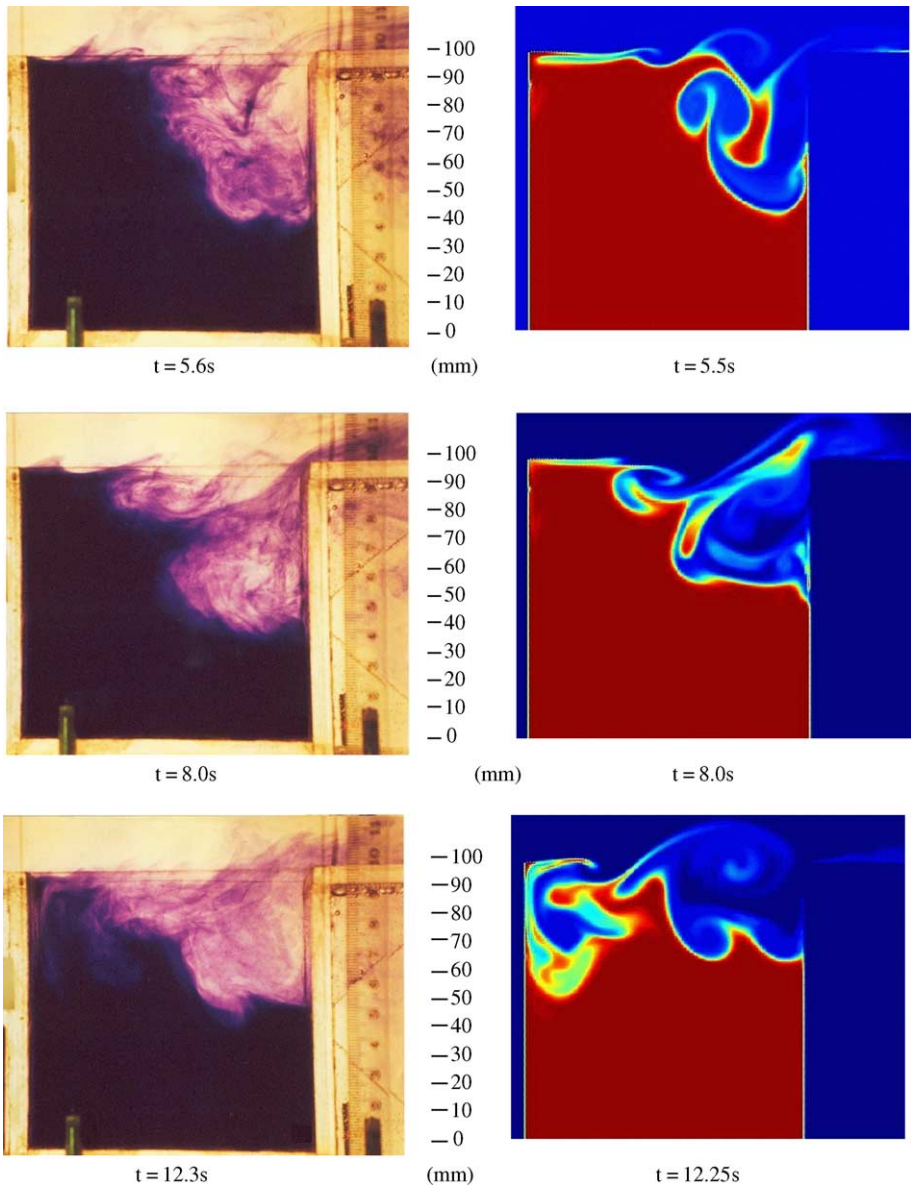

Fig. 5. Stage 2: experimental and 2D numerical solute fields.

the dominant mechanism of turbulent entrainment in shear-free density surfaces. This finding is supported by the experimental results of McGrath et al. [4], although they found eddy impingement to be the dominant transport mechanism only at low flux Richardson numbers. The Froude number (see Eq. (3)) for the purging flow presented here is $Fr = 2.2$, so the local flux Richardson number is expected to be low, typically of order 1. While there is also shear present in the purging cavity flow, this shear decreases as the interface drops. Thus we might expect eddy impingement to be an important transport mechanism in the present case.

The visualisations provide qualitative support for this theory. In both the experimental and numerical images, impinging eddies are seen apparently deflecting the interface and causing ejections of salt water into the fresh water above. A more conclusive argument, however, is based on the observation that, in the case of the purging cavity, the impinging eddies are essentially two-dimensional. If eddy impingement is in fact the dominant transport mechanism, then we would expect the 2D simulation to give a good representation of the purging process during this stage. This is indeed the case. Not only do the flow visualisations show a

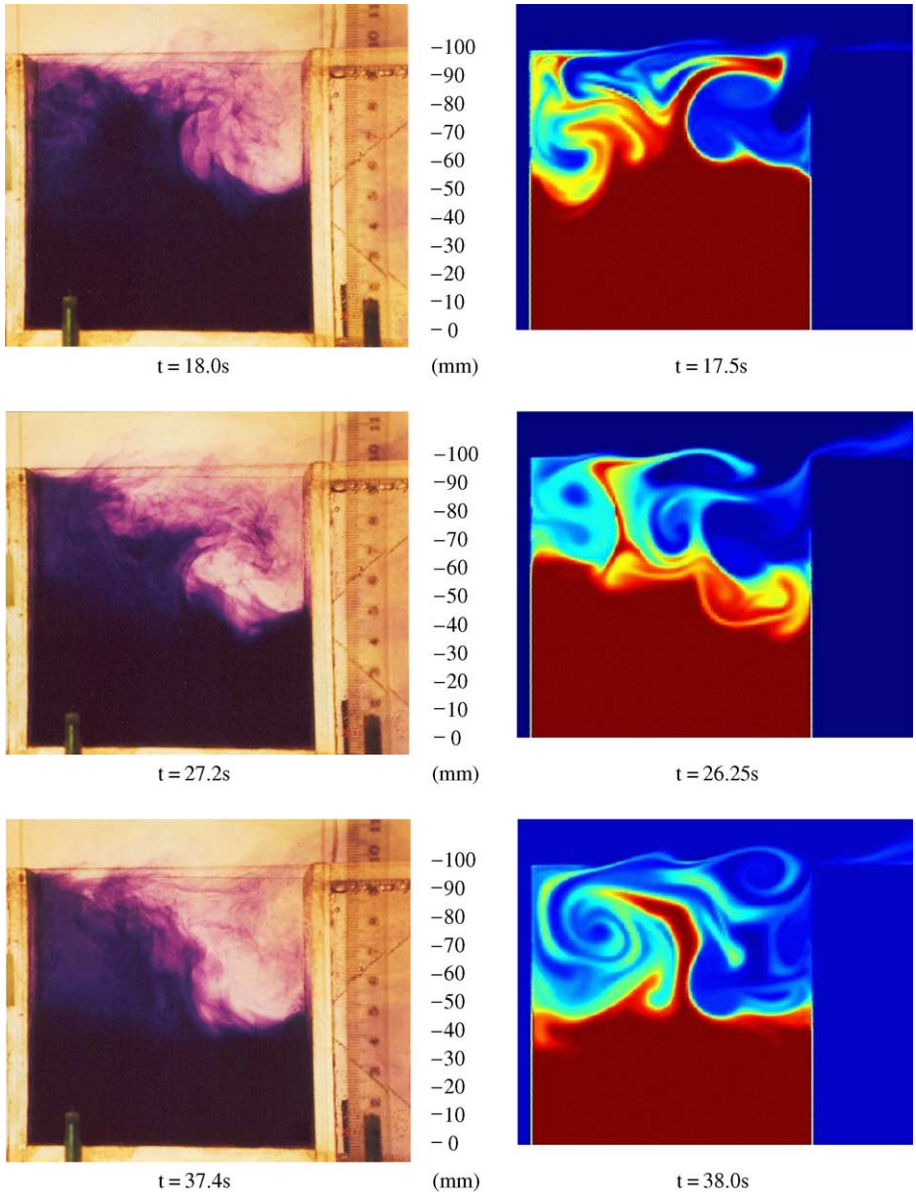

Fig. 6. Stage 2 continued: experimental and 2D numerical solute fields.

remarkable level of qualitative agreement, but, as discussed in Section 4.1, the purging rate predicted by the simulation is also in excellent quantitative agreement with the experiment during this stage. Thus we conclude, that eddy impingement appears to be the dominant transport mechanism during Stage 3.

It is also interesting to note that, in the case of the purging cavity, because the impinging eddies are two-dimensional, the eddy impingement mechanism is essentially a laminar rather than a turbulent process.

4.2.4. Stage 4: t = 100–200 s

Fig. 8 shows the numerical and experimental solute fields during Stage 4, corresponding to the time interval $t = 100$–200 s. By this stage, the large clockwise-rotating vortex on the RHS dominates flow within the cavity. The vortex rotates slowly, carrying with it typically four or five of the smaller spanwise vortices generated at the top of the cavity. While in the previous stage these smaller vortices, were found to be primarily responsible for lifting denser fluid across the interface through the eddy impingement mechanism, in Stage 4 the mechanism appears to change. During this stage

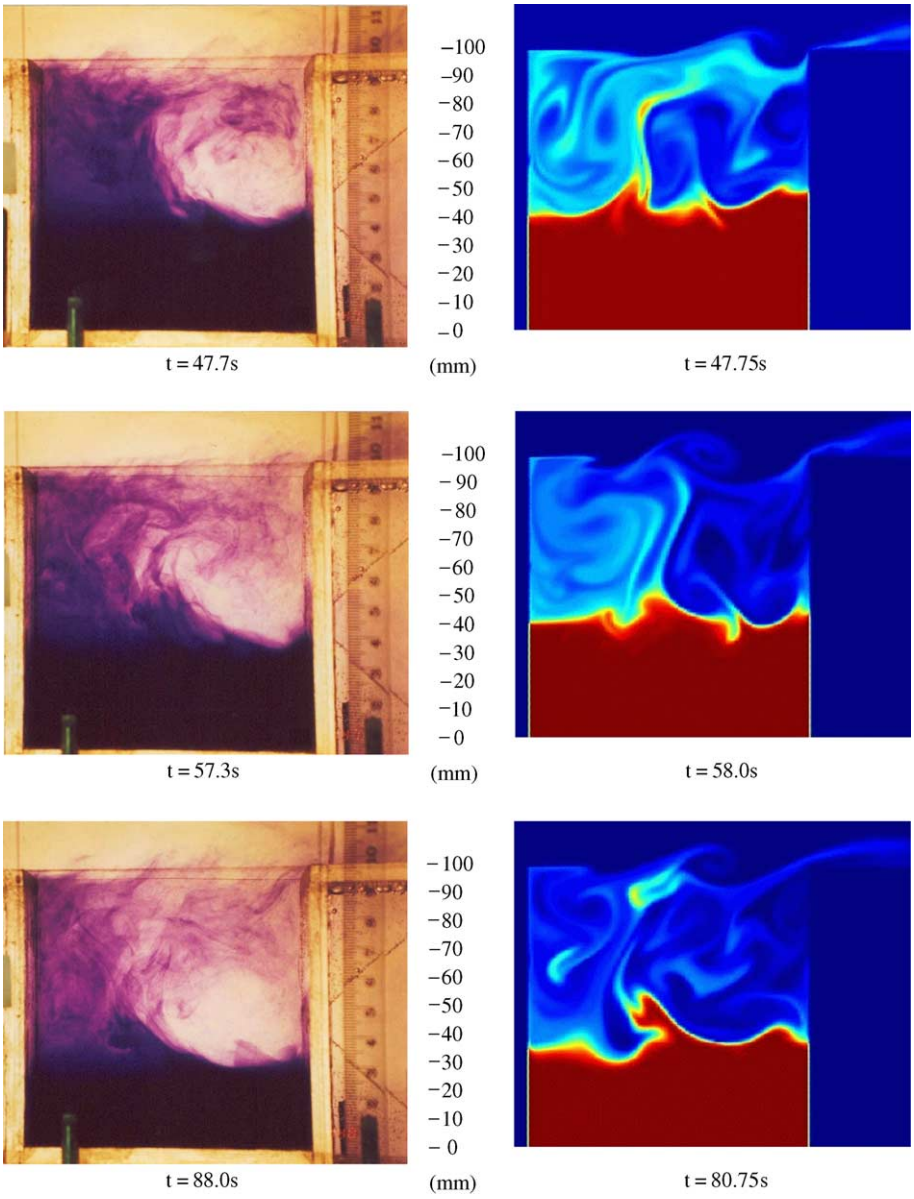

Fig. 7. Stage 3: experimental and 2D numerical solute fields.

wave-like structures are seen travelling along the interface from right to left. As discussed in the introduction, streamers ejected from the crests of the waves are believed to be the dominant entrainment mechanism during this stage. The experimental visualisation at $t = 117.5$ s shows an example of one of the streamers, identified as a fine, 'wispy' structure, drawn out from the crest of a wave.

The streamers typically originate from a localised point source, rather than from a line along the crest of the waves, implying that the formation of the streamers is a three-dimensional turbulent process. The 2D simulation must therefore rely on the turbulence model to parameterise this transport mechanism. As can be seen from the visualisations, streamer-like structures are being formed in the numerical simulation. As shown in Section 4.1, however, quantitatively the simulation is underpredicting the entrainment rate by approximately 30%. A possible mechanism for generating the streamers is presented in combination with the 3D large eddy simulation results in the next section.

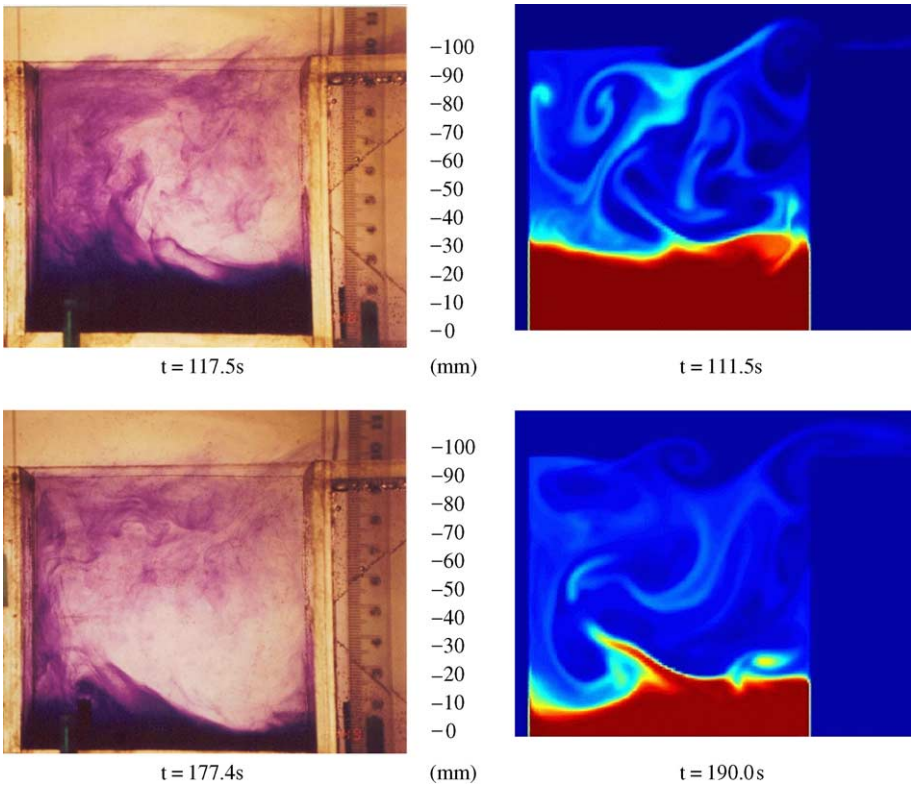

Fig. 8. Stage 4: experimental and 2D numerical solute fields.

5. Large eddy simulation results

In this section, the simulation of Stage 4 is repeated in three dimensions. The aims of this section are two-fold. Firstly we investigate the effect of including the three-dimensional turbulent structures in the simulation on the prediction of the purging rate. Secondly, we analyse the flow fields generated during the 3D simulation and use these to propose a mechanism for the formation of the streamers. To reduce the computation time, the simulation is started from the 2D solution at $t = 100$ s. Fig. 9 shows a time series of the spanwise velocity component taken at the point (0,70,−70)mm for $t = 100$–200 s. The signal grows over $t = 100$–140 s after which it remains within a range of $u_{max} \pm 0.0075$ m/s. The three-dimensional flow is therefore considered fully evolved by $t = 140$ s.

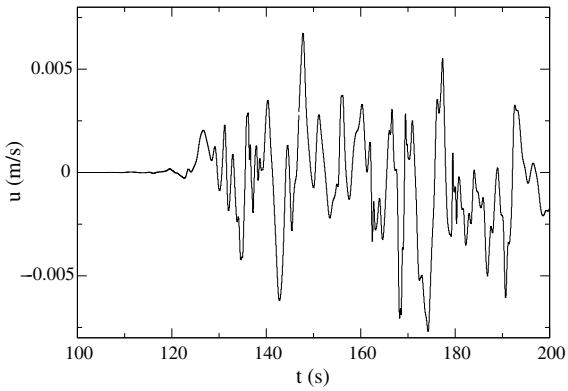

Fig. 9. Time series of spanwise velocity component for Stage 4.

5.1. Comparison of purging rate

Fig. 10 shows a comparison of the 2D and 3D numerical results for H and Q for $t = 100$–200 s. As stated above, estimating purging rate using dH/dt and dQ/dt gives a similar result during Stage 4. Since dQ/dt can be calculated more accurately, this parameter is used here for comparison of the two sets of results. For $t = 100$–125 s the flow remains essentially two-dimensional and the 2D and 3D results for Q overlay one another. For $t = 125$–140 s the curves diverge slightly, with dQ/dt lower in the 3D simulation. It appears that during this period processes involved in the transition from 2D flow to 3D turbulent flow are extracting energy from the flow structures responsible for interfacial mixing,

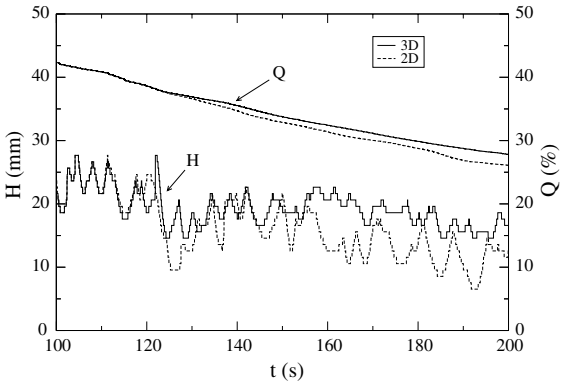

Fig. 10. Comparison of 2D and 3D numerical results for interface height H and the amount of solute remaining in the cavity Q during Stage 4.

leading to a decrease in the purging rate. By $t = 140$ s the turbulent flow is fully developed and dQ/dt for the 3D simulation increases again to a value similar to that given by the 2D simulation. The two curves remain parallel up until $t = 180$ s after which the purging rate predicted by the 2D simulation is slightly higher than that of the 3D simulation. The mean purging rate for Stage 4 in the 3D simulation as calculated for $t = 140$–200 s is 0.14%/s. Reasons for this unexpected result will be suggested in the next section, following a discussion of the structure of the flow field and a possible mechanism for the formation of the streamers.

5.2. Flow field structure

Fig. 11 shows two three-dimensional views of the interface at $t = 170$ s. The most prominent feature of the surface is a wave close to the mid-point of the cavity. The interface is also significantly deformed in the spanwise direction. This deformation is particularly noticeable at the crest of the wave, which rises to a sharp peak rather than remaining relatively horizontal as might have been expected.

Fig. 12 shows a yz-section through the velocity and concentration fields at this time. Above the interface, there is a large vortex circulating fluid of low solute concentration and filling approximately two-thirds of the cavity. The relatively low velocities below the interface are evidence of the stabilising effect of buoyancy force resulting from the density stratification. Also apparent in the figure is one of the smaller spanwise vortices generated in the shear layer at the top of the cavity. This layer contains both a velocity and a density gradient, and the vortices have the appearance of Kelvin–Helmholtz billows.

These spanwise vortices are seen more clearly in Fig. 13 which shows a three-dimensional view of vorticity in the cavity at $t = 170$ s. On reaching the downstream wall of the cavity, the vortices are split by the sharp corner and the lower part of each vortex is deflected down into the cavity where it joins the large scale circulation. Meanwhile the upper part is convected away by the overflow. In this figure, four of these vortices are visible. In addition to the vortex at the downstream end of the shear layer at the top of the cavity, there are two vortices moving down the cavity wall while one is moving back across the cavity a small distance above the interface.

Also of interest in Fig. 13 is a vortex sheet associated with the turbulent boundary layer on the downstream wall of the cavity. This vortex sheet detaches from the wall above the interface and is convected along the top of the interface by the circulating fluid. The xz-section through the vorticity and velocity fields shows a pair of counter-rotating vortices deforming the sheet. This type of structure is a characteristic feature of turbulent boundary layers as demonstrated in the experimental investigations of Willmarth and Tu [33], Clark and Markland [34] and Eckelmann [35] and the DNS results of Jiménez and Moin [36] among others. The vortex-pair has a width of $x^+ \approx 100$ based on the mean wall shear stress, which is consistent with the mean velocity streak spacing observed by Smith and Metzler in turbulent channel flow [22]. Velocity streaks observed in the laminar sublayer of turbulent boundary layers are associated with pairs of counter-rotating streamwise vortices, which lift low-momentum fluid away from the wall and carry it into the core flow. In the present case, a juxtaposition of Figs. 11 and 13 shows the streamwise vortices distorting the interface. In particular, the two figures show the wave crest being lifted to a sharp peak by the fluid carried up between the two vortices. (In Fig. 13 this region between the two vortices crosses the periodic boundaries on either side of the domain.)

The observations described above lead us to propose a mechanism for the formation of streamers. The mechanism depends on the presence of three features: interfacial waves, counter-rotating streamwise vortices and small eddies in the turbulent boundary layer above the interface. In the case of the purging cavity, interfacial waves are clearly present in both the experiment and simulations. While the source of the waves is not important for the streamer formation, a possible mechanism in the case of the cavity flow involves excitation by a periodic forcing provided by the spanwise vortices circulating in the cavity. A turbulent boundary layer containing counter-rotating streamwise vortices is also shown in the LES results forming on the downstream cavity wall and above the interface. As fluid moves upward between the streamwise vortices it deforms the interface, and lifts the crest of the wave, forming a sharp spanwise peak. Close to the peak the steep gradient of the interface reduces the component of the gravitational force normal to the interface, which reduces the restoring

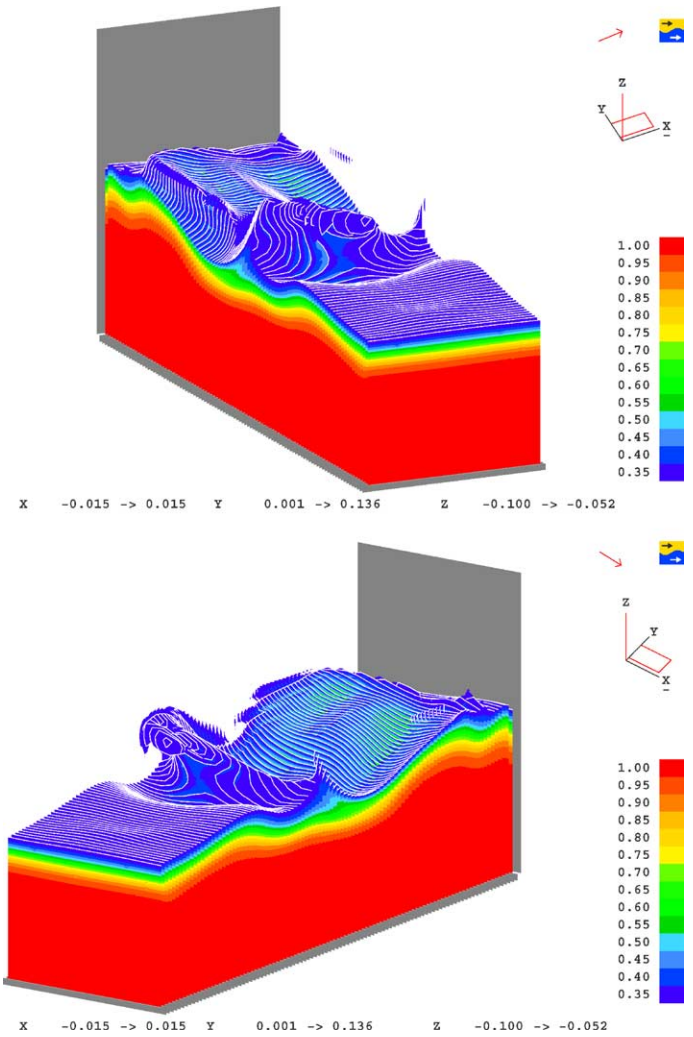

Fig. 11. 3D simulation of Stage 4: Three-dimensional views of the interface at $t = 170$ s showing c iso-surfaces from $c = 0.35$ to 1.0. The two views look downstream and are taken from left- and right-hand sides of the cavity.

buoyancy force and hence reduces the energy required for the turbulent eddies to entrain dense fluid. As a result, a thin streamer is formed as fluid is entrained from either side of the peak of the wave by smaller turbulent eddies. The stream of dense fluid remains relatively coherent as it is transported through the narrow region between the two streamwise vortices. Once it reaches the upper side of the vortices it is ejected into the less coherent turbulent flow field above where it tends to diffuse rapidly. This can be seen in the experimental visualisation at $t = 117$ s shown in Fig. 8.

While the 3D simulation proved useful in enabling us to visualise the flow fields and formulate this hypothesis, no obvious streamers were formed in the simulation. The streamers observed in the experiment were typically less than 1 mm across, which is well below the resolution of the simulation. On the other hand, the simulation does capture two of the three critical features required by the mechanism described above, namely the interfacial waves, and the counter-rotating streamwise vortices. The third feature, the small boundary layer eddies that actually do the work of entraining the dense fluid, are resolved only poorly if at all. Their effect, however, should be parameterised by the subgrid turbulence model in the form of a high local eddy viscosity and diffusivity close to the interface.

Fig. 14 shows a yz-section through the eddy viscosity field. For reference, the solute concentration field is also shown. The eddy viscosity is normalised by the molecular viscosity $\nu^*_{\mathrm{sgs}} = \nu_{\mathrm{sgs}}/\nu$. While there is a region of increased eddy viscosity over the interface behind the crest of the wave, and also in the fluid above the

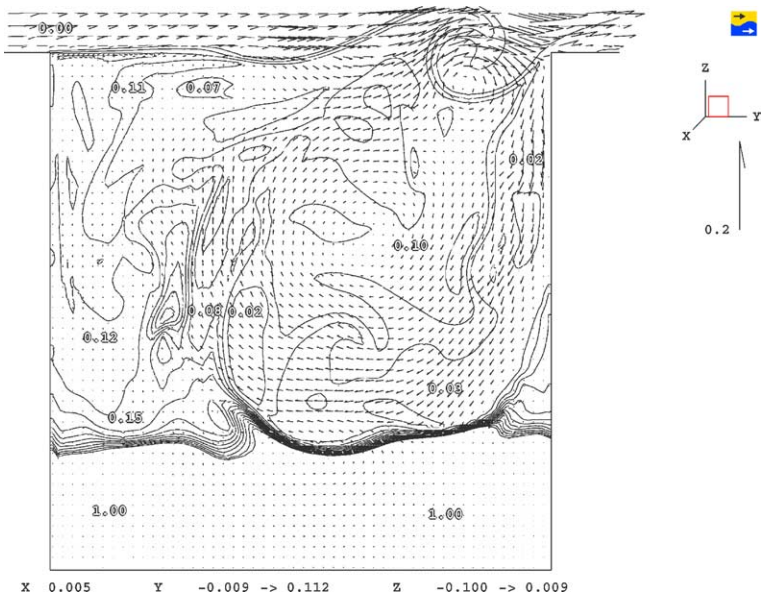

Fig. 12. 3D simulation of Stage 4: A *yz*-section through the concentration and velocity fields at $t = 170$ s. Solute concentration is presented in normalised form, c.

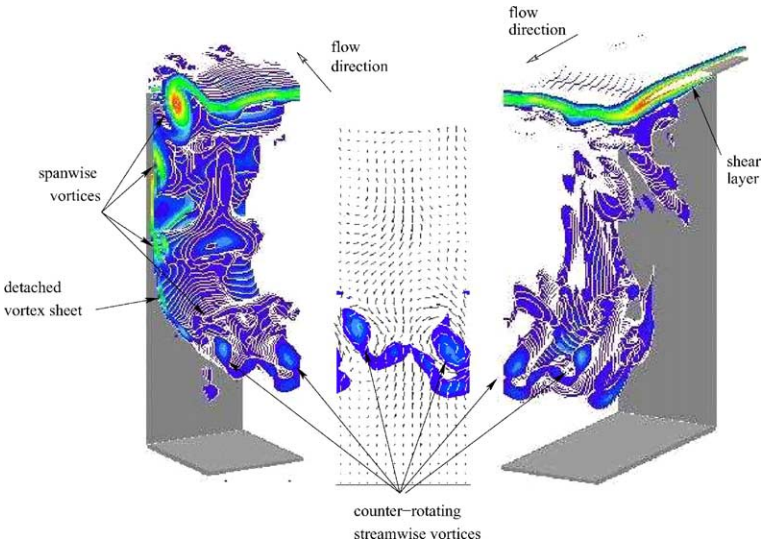

Fig. 13. 3D simulation of Stage 4: Vorticity field in the cavity at $t = 170$ s. The two three-dimensional views look downstream and upstream from an *xz*-plane at $y = 66$ mm. Vorticity is visualised as iso-contours of $|\boldsymbol{\omega}|$. The section view looks downstream and shows velocity vectors superimposed on the vorticity field in the *xz*-plane at $y = 66$ mm.

wave, close to the wave crest itself, the eddy viscosity is relatively low. This unexpected behaviour is explained by noting that the eddy viscosity is negative just below the interface, indicating that the dynamic procedure is calculating a negative model coefficient at points just below the interface. As described in Section 3.2 it was found necessary to average the model coefficient in the spanwise direction to maintain numerical stability. In retrospect, however, it appears that this approach is not appropriate for this type of flow, as a typical spanwise line close to the wave crest will contain points both above and below the interface. Consequently positive values of the model coefficient calculated at points above the surface will be cancelled out by negative values at points below the surface. The result is an underprediction of the eddy diffusivity

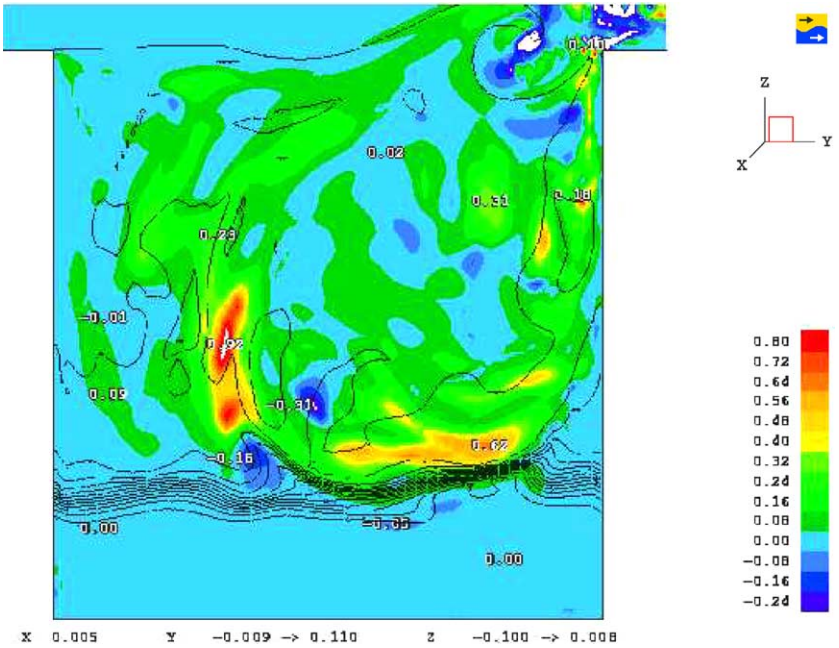

Fig. 14. 3D simulation of Stage 4: yz-sections through the eddy-viscosity field at $t = 170$ s. The filled contours represent the eddy viscosity, with values shown at various locations. The black lines overlaid on the plot are iso-contours of solute concentration. Eddy viscosity is normalised, $\nu^*_{sgs} = \nu_{sgs}/\nu$.

parameterising the small turbulent eddies in the critical region close to the wave crest. Without the effect of these eddies, the model fails to produce the streamers, in spite of successfully generating the other two components of the streamer mechanism, namely the interfacial waves and streamwise vortices. The end result is that the large eddy simulation underpredicts the purging rate.

6. Conclusions

Experimental and numerical results have been presented for a flow in which salt water is purged from a square cavity by an overflow of fresh water. The results have been used to describe the important transport mechanisms occurring during the purging process and to assess the performance of the numerical model for flows of this type.

The purging process is divided into four stages based on the dominant transport mechanisms observed at different times during the course of the numerical and physical experiments. A 2D simulation was performed for the entire purging process. While the turbulent flow field cannot be captured in two dimensions, the 2D simulation accurately reproduces the large-scale flow structures observed in the experiment, with excellent qualitative agreement seen between the experimental and numerical results during all stages. While differences in initial conditions make comparison of purging rates during the initial stages difficult, it is possible to compare purging rates during Stages 3 and 4.

During Stage 3, the agreement between purging rate measured in the experiment and that predicted by the 2D simulation is excellent, with the numerical results overlaying the experimental data points. Since the simulation is two-dimensional, such a high level of agreement indicates that the primary transport mechanism during this stage is also essentially two-dimensional. This supports our claim that the dominant transport mechanism during Stage 3 involves eddy impingement by 2D spanwise vortices formed in the stratified shear layer at the top of the cavity. Eddy impingement has been found by other researchers to be the dominant mechanism for turbulent entrainment across a sharp density interfaces at low Richardson numbers. In the present case, because the impinging eddies are basically two-dimensional, this process could be considered to be a laminar rather than a turbulent process.

Agreement during Stage 4 is not as good, although the purging rate of 0.16%/s predicted by the simulation is still within 30% of the experimental result of 0.23%/s. This is a significant improvement over unsteady RANS simulations, which overpredict the purging rate by an order of magnitude, and 2D DNS, which underpredicts

it by a similar degree. Nevertheless, it appears that the 2D simulation was unable to capture the streamers observed in the experiment. The streamers are ejected from the crests of interfacial waves and appear to play an important role in the purging process during this stage.

A three-dimensional large eddy simulation of Stage 4 was performed to investigate the nature of the three-dimensional flow field during this stage. Based on observations from the LES results, a mechanism was proposed for the formation of the streamers. The mechanism involves the interaction of interfacial waves, counter-rotating streamwise vortices in the boundary layer above the interface, and small turbulent eddies close to the wave crest. The LES simulation predicts the waves and streamwise vortices, but does not adequately parameterise the small eddies. This was found to be due to the spanwise averaging in the dynamic procedure used to calculate the coefficient in the turbulence model. As a result the LES is unable to represent the effect of the streamers and also underpredicts the purging rate.

These results serve to highlight the importance of the subgrid scale turbulence model in large eddy simulations. They also highlight problems associated with the need to using averaging methods in order to stabilise the dynamic Smagorinsky model. While this averaging approach is adequate for relatively simple flows such as channel flow, it has been shown here that it is not appropriate for flows involving a sharp interface that experiences significant deflections.

A further study is necessary to test the proposed mechanism for streamer formation described above. This study may use either a direct numerical simulation of the same flow, or another LES, with an improved SGS model that does not involve spatial averaging of the model coefficient.

Acknowledgments

The first author gratefully acknowledges the support of the Australian Research Council. The authors also thank Professor John Kent at The University of Sydney for the visualisation software SHOW3D used to produce the images from the computer simulations.

References

[1] W.D. Smyth, J.N. Moum, Anisotropy of turbulence in stably stratified mixing layers, Phys. Fluids 12 (6) (2000) 1343–1362.

[2] W.D. Smyth, J.N. Moum, Length scales of turbulence in stably stratified mixing layers, Phys. Fluids 12 (6) (2000) 1327–1342.

[3] H.J.S. Fernando, J.C.R. Hunt, Turbulence, waves and mixing at shear-free density interfaces. Part 1. A theoretical model, J. Fluid Mech. 347 (1997) 197–234.

[4] J.L. McGrath, H.J.S. Fernando, J.C.R. Hunt, Turbulence, waves and mixing at shear-free density interfaces. 2. Laboratory experiments, J. Fluid Mech. 347 (1997) 235–261.

[5] M.C. Gregg, Dyapycnal mixing in the thermocline: a review, J. Geophys. Res.—Oceans 92 (C5) (1987) 5249–5286.

[6] H.J.S. Fernando, Turbulent mixing in stratified fluids, Ann. Rev. Fluid Mech. 23 (1991) 455–493.

[7] D.R. Caldwell, J.N. Moum, Turbulence and mixing in the ocean, Rev. Geophys. 33 (pt. 2) (1995) 1385–1394.

[8] J. Riley, M. Lelong, Fluid motions in the presence of strong stable stratification, Ann. Rev. Fluid Mech. 32 (2000) 613–657.

[9] J.R. Anderson, A.K. Morrison, Environmental flow studies for the Wimera, Victoria, Tech. Rep. Series Nos. 73–78, Arthur Rylah Institute for Environmental Research, Department of Conservation, Forests and Lands, Victoria, Australia, 1989.

[10] J.T. McGuckin, Environmental considerations of salinity in the Goulbourn river downstream of Shepparton, Tech. Rep. Series Nos. 118, Arthur Rylah Institute for Environmental Research, Department of Conservation, Forests and Lands, Victoria, Australia, 1991.

[11] M. Gill, Hydromechanics of mining pits in erodible bed under steady flow, ASCE J. Hydr. Eng. 120 (1994) 337–348.

[12] P. Prinos, V. Dermissis, Interfacial resistance and mixing in stratified channel flows, in: 4th Int. Symp. on Stratified Flows, Grenoble, France, June 29–July 2, 1994.

[13] G. Abraham, in: Turbulence and Mixing in Stratified Tidal Flows, Physical Processes in Estuaries, Springer-Verlag, 1988, pp. 149–180.

[14] W. Debler, J. Imberger, Flushing criteria in estuarine and laboratory experiments, ASCE J. Hydr. Eng. 122 (12) (1996) 728–734.

[15] S.W. Armfield, W. Debler, Purging of density stabilized basins, Int. J. Heat Mass Transfer 36 (1993) 519–530.

[16] W. Debler, S.W. Armfield, The purging of saline water from rectangular and trapezoidal cavities by an overflow of sweet water, J. Hydraulic Res. 35 (1997) 43–62.

[17] T.J. Craft, N.Z. Ince, B.E. Launder, Recent developments in second moment closure for buoyancy-affected flows, Dyn. Atm. Oceans 23 (1996) 99–114.

[18] M.P. Kirkpatrick, A large eddy simulation code for industrial and environmental flows, Ph.D. thesis, The University of Sydney, 2002.

[19] J. Smagorinsky, General circulation experiments with the primitive equations, I. The basic experiment, Mon. Weath. Rev. 91 (1963) 99–164.

[20] M. Germano, U. Piomelli, P. Moin, W.H. Cabot, A dynamic subgrid-scale eddy viscosity model, Phys. Fluids A 3 (7) (1991) 1760–1765.

[21] S.J. Kline, W.C. Reynolds, F.A. Schraub, P.W. Runstadler, The structure of the turbulent boundary layer, J. Fluid Mech. 30 (1967) 741–773.

[22] C.R. Smith, S.P. Metzler, The characteristics of low-speed streaks in the near wall region of a turbulent boundary layer, J. Fluid Mech. 129 (1983) 27–54.
[23] H. Werner, H. Wengle, Large eddy simulation of turbulent flow over and around a cube in a plate channel, in: F. Durst, R. Friedrich, B.E. Launder, F.W. Schmidt, U. Schumann, J.H. Whitelaw (Eds.), Turbulent Shear Flows 8, Springer-Verlag, 1993, pp. 155–168.
[24] B.P. Leonard, Sharp simulation of discontinuities in highly convective steady flow, NASA Technical Memorandum 100240 (1987).
[25] M.P. Kirkpatrick, S.W. Armfield, J.H. Kent, A representation of curved boundaries for the solution of the Navier–Stokes equations on a staggered three-dimensional Cartesian grid, J. Comp. Phys. 184 (2003) 1–36.
[26] M. Breuer, Numerical and modeling influences on large eddy simulations for the flow past a circular cylinder, Int. J. Heat Fluid Flow 19 (1998) 512–521.
[27] J. Van Kan, A second order accurate pressure correction scheme for viscous incompressible flow, SIAM J. Sci. Stat. Comput. 7 (1986) 870–891.
[28] J.B. Bell, P. Colella, H.M. Glaz, A second-order projection method for the incompressible Navier–Stokes equations, J. Comp. Phys. 85 (1989) 257–283.
[29] S.W. Armfield, R. Street, The fractional-step method for the Navier–Stokes equations on staggered grids: the accuracy of three variations, J. Comp. Phys. 153 (1999) 660–665.
[30] P. Gresho, On the theory of semi-implicit projection methods for viscous incompressible flow and its implementation via finite element method that also introduces a nearly consistent mass matrix. Part 1: Theory, Int. J. Numer. Meth. Fluids (1990) 587–620.
[31] M.P. Kirkpatrick, S.W. Armfield, J.H. Kent, T. Dixon, Simulation of vortex-shedding flows using high-order fractional step methods, J. Anziam 42 (E) (2000) 856–876.
[32] P.F. Linden, The interaction of vortex rings with a sharp density interface: a model for turbulent entrainment, J. Fluid Mech. 60 (1973) 467–480.
[33] W.W. Willmarth, B.J. Tu, Structure of turbulence in the boundary layer near the wall, Phys. Fluids 10 (1967) S134–S137.
[34] J.A. Clark, E. Markland, Flow visualization in turbulent boundary layers, J. Hydraul. Div. ASCE 97 (1971) 1635–1664.
[35] H. Eckelmann, The structure of the viscous sublayer and the adjacent wall region in a turbulent channel flow, J. Fluid Mech. 65 (1974) 439–459.
[36] J. Jiménez, P. Moin, The minimal flow unit in near-wall turbulence, J. Fluid Mech. 225 (1991) 213–240.